Imidazolium Ionic Liquid Crystals with Pendant Mesogenic Groups

Karel Goossens,[†] Peter Nockemann,[†] Kris Driesen,[†] Bart Goderis,[†] Christiane Görller-Walrand,[†] Kristof Van Hecke,[†] Luc Van Meervelt,[†] Eric Pouzet,[‡] Koen Binnemans,[†] and Thomas Cardinaels*[,†]

Department of Chemistry, Katholieke Universiteit Leuven, Celestijnenlaan 200F, bus 2404, B-3001 Leuven, Belgium, and Laboratoire de Chimie des Polymères CP 206/1, Université Libre de Bruxelles, Boulevard du Triomphe, B-1050 Bruxelles, Belgium

Received August 16, 2007

Ionic liquid crystals were obtained by coupling one or two mesogenic units (cholesterol or cyanobiphenyl) to an imidazolium cation. Anions are bromide, bis(trifluoromethylsulfonyl)imide, and tetrakis(2-thenoyltrifluoroacetonato)europate(III). The mesomorphism of the compounds depends on the type and number of mesogenic units and on the type of anion. In general, the most stable mesophases are observed for the bis(trifluoromethylsulfonyl)imide salts. Most of the compounds containing cholesterol moieties show enantiotropic SmA* phases over a broad temperature range, and some of them are room temperature liquid crystals. Modeling of the small-angle X-ray scattering patterns revealed the molecular arrangement in these mesophases. On the contrary, most of the compounds containing cyanobiphenyl groups exhibit monotropic lamellar or nematic mesophases, depending on the number of mesogenic units. The imidazolium salts containing the tetrakis(2-thenoyltrifluoroacetonato)europate(III) anion show an intense red photoluminescence.

Introduction

Ionic liquids are organic salts with a melting point below 100 °C.[1–3] They are intensively investigated because of their applications in solvents for organic reactions,[4,5] extraction solvents,[6–8] electrolytes for fuel cells[9,10] or solar cells,[11,12] and electrolytic media for electrodeposition of reactive metals.[13–15] Ionic liquids are also useful as templating agents for the synthesis of inorganic nanostructures.[16–20] Although many organic cations can be used for the design of ionic liquids, none of these cations are as popular as the imidazolium ion. Typical examples of imidazolium ionic liquids are 1-ethyl-3-methylimidazolium hexafluorophosphate and 1-butyl-3-methylimidazolium bis(trifluoromethylsulfonyl)-imide.[21] Recently, a series of imidazolium-based lanthanide-containing ionic liquids have been reported to be liquid at room temperature.[22] The melting points of 1,3-dialkylimidazolium salts depend not only on the anion but also on the number of carbon atoms in the alkyl chains.[23] It is observed for 1-alkyl-3-methylimidazolium salts that the melting point first decreases with increasing alkyl chain length. After a minimum is reached (typically for hexyl, heptyl, or octyl chains), the melting point starts to rise with increasing chain length. Interestingly, for 1-alkyl-3-methylimidazolium salts with long alkyl chains, a liquid-crystal phase (mesophase) is observed, and the mesophase stability rapidly increases with increase in the alkyl chain length.[23–26] The minimum length of the alkyl chain for which a mesophase is observed depends on the anion, but it seems to be a rule that at least a dodecyl chain is required. Without exception, the long-

* Corresponding author. E-mail: thomas.cardinaels@chem.kuleuven.be.
† Katholieke Universiteit Leuven.
‡ Université Libre de Bruxelles.

(1) Seddon, K. R. J. *Chem. Technol. Biotechnol.* **1997**, *68*, 351–356.
(2) Wasserscheid, P.; Keim, W. *Angew. Chem., Int. Ed.* **2000**, *39*, 3773–3789.
(3) Welton, T. *Chem. Rev.* **1999**, *99*, 2071–2083.
(4) Dupont, J.; de Souza, R. F.; Suarez, P. A. Z. *Chem. Rev.* **2002**, *102*, 3667–3691.
(5) Welton, T. *Coord. Chem. Rev.* **2004**, *248*, 2459–2477.
(6) Visser, A. E.; Swatloski, R. P.; Griffin, S. T.; Hartman, D. H.; Rogers, R. D. *Sep. Sci. Technol.* **2001**, *36*, 785–804.
(7) Visser, A. E.; Swatloski, R. P.; Reichert, W. M.; Mayton, R.; Sheff, S.; Wierzbicki, A.; Davis, J. H.; Rogers, R. D. *Chem. Commun.* **2001**, 135–136.
(8) Huddleston, J. G.; Willauer, H. D.; Swatloski, R. P.; Visser, A. E.; Rogers, R. D. *Chem. Commun.* **1998**, 1765–1766.
(9) Shin, J. H.; Henderson, W. A.; Passerini, S. *J. Electrochem. Soc.* **2005**, *152*, A978–A983.
(10) Nakagawa, H.; Izuchi, S.; Kuwana, K.; Nukuda, T.; Aihara, Y. *J. Electrochem. Soc.* **2003**, *150*, A695–A700.
(11) Grätzel, M. *J. Photochem. Photobiol., C* **2003**, *4*, 145–153.
(12) Papageorgiou, N.; Athanassov, Y.; Armand, M.; Bonhôte, P.; Pettersson, H.; Azam, A.; Grätzel, M. *J. Electrochem. Soc.* **1996**, *143*, 3099–3108.
(13) Endres, F. *Z. Phys. Chem.* **2004**, *218*, 255–283.
(14) Endres, F.; Bukowski, M.; Hempelmann, R.; Natter, H. *Angew. Chem., Int. Ed.* **2003**, *42*, 3428–3430.
(15) Endres, F. *ChemPhysChem* **2002**, *3*, 144–154.
(16) Antonietti, M.; Kuang, D. B.; Smarsly, B.; Yong, Z. *Angew. Chem., Int. Ed.* **2004**, *43*, 4988–4992.
(17) Taubert, A.; Steiner, P.; Mantion, A. *J. Phys. Chem. B* **2005**, *109*, 15542–15547.
(18) Taubert, A. *Angew. Chem., Int. Ed.* **2004**, *43*, 5380–5382.
(19) Taubert, A. *Acta Chim. Slov.* **2005**, *52*, 183–186.
(20) Taubert, A.; Li, Z. *Dalton Trans.* **2007**, 723–727.
(21) Bonhôte, P.; Dias, A. P.; Papageorgiou, N.; Kalyanasundaram, K.; Grätzel, M. *Inorg. Chem.* **1996**, *35*, 1168–1178.
(22) Nockemann, P.; Thijs, B.; Postelmans, N.; Van Hecke, K.; Van Meervelt, L.; Binnemans, K. *J. Am. Chem. Soc.* **2006**, *128*, 13658–13659.
(23) Gordon, C. M.; Holbrey, J. D.; Kennedy, A. R.; Seddon, K. R. *J. Mater. Chem.* **1998**, *8*, 2627–2636.
(24) Binnemans, K. *Chem. Rev.* **2005**, *105*, 4148–4204.
(25) Bowlas, C. J.; Bruce, D. W.; Seddon, K. R. *Chem. Commun.* **1996**, 1625–1626.
(26) Bradley, A. E.; Hardacre, C.; Holbrey, J. D.; Johnston, S.; Mcmath, S. E. J.; Nieuwenhuyzen, M. *Chem. Mater.* **2002**, *14*, 629–635.

10.1021/cm702321c CCC: $40.75
Published on Web 12/11/2007

chain 1-alkyl-3-methylimidazolium salts exhibit smectic mesophases. Here, the molecules are arranged into layers due to the electrostatic interactions between the ionic constituents of these ionic liquid crystals. Nematic phases are very uncommon for ionic liquid-crystalline systems.[24] Ionic liquid crystals based on imidazolium and other organic salts have recently been reviewed by Binnemans.[24] This review shows that the most common method for obtaining ionic liquid crystals is the attachment of long alkyl chains to the ionic liquid cation. Among the exceptions are the salts where a mesogenic group is closely connected to the imidazolium[27–30] or pyridinium core[31] and imidazolium[32–37] and pyridinium[38–42] salts with a mesogenic group linked via a long alkyl spacer to the heterocyclic cation. Ionic liquid crystals are of interest because they show anisotropic ionic conduction and because they allow to obtain organized molecular materials.[28,30,43,44] Metal-containing ionic liquid crystals (*ionic metallomesogens*) are a special class of ionic liquid crystals, which combine the properties of metal ions, ionic liquids, and liquid crystals.[24,45–50] These compounds are presently investigated by several research groups because the decomposition of the metal-containing moiety in the mesophase leads to the formation of inorganic materials (e.g., CuCl, gold, and silver nanoparticles) with an unusual morphology.[17–20,51–55] Ionic lanthanide-based metallomesogens (lanthanidomesogens) offer the possibility to obtain magnetic or luminescent liquid crystals.[56–64]

In this paper, a nonconventional approach toward liquid-crystalline imidazolium salts is presented. Mesophase promoters like the cholesterol and cyanobiphenyl group are attached via a long flexible chain to an imidazolium core. This approach allows incorporating bulky molecular units into ionic liquid crystals and consequently to create luminescent ionic liquid crystals. Unexpectedly, this method also allows obtaining nematogenic ionic liquid crystals.

Experimental Section

General Procedures. Nuclear magnetic resonance (NMR) spectra were recorded on a Bruker Avance 300 spectrometer (operating at 300 MHz for ^{1}H) or a Bruker AMX-400 spectrometer (operating at 400 MHz for ^{1}H). FTIR spectra were recorded on a Bruker IFS-66 spectrometer, using the KBr pellet method. Elemental analyses were obtained on a CE Instruments EA-1110 elemental analyzer. Electrospray ionization (ESI) mass spectra were recorded on a Thermo Finnigan LCQ Advantage mass spectrometer. Optical textures of the mesophases were observed with an Olympus BX60 polarizing microscope equipped with a LINKAM THMS600 hot stage and a LINKAM TMS93 programmable temperature controller. DSC traces were recorded with a Mettler-Toledo DSC822e module. Powder X-ray diffraction patterns were recorded with a Bruker AXS D8 Advance diffractometer mounted with a copper X-ray ceramic tube, working at 1.6 kW. The emitted Cu Kα radiation ($\lambda = 1.5418$ Å) was focused on the sample by a Göbel mirror. All the samples were prepared by spreading the powders on a thin cleaned aluminum plate. Diffraction patterns were collected using the Bragg–Brentano reflection geometry ($\theta/2\theta$ setup) at an angular resolution (in 2θ) of 0.02° per step. The sample temperature was controlled within an accuracy of 0.1 °C. The scattered signal was recorded by a scintillation counter. X-ray diffractograms are represented as the logarithm of the scattering intensity (in counts per second) versus the scattering angle, 2θ. Photoluminescence spectra were recorded on an Edinburgh Instruments FS900 spectrofluorimeter. This instrument is equipped with a xenon arc lamp, a microsecond

(27) Dobbs, W.; Douce, L.; Allouche, L.; Louati, A.; Malbosc, F.; Welter, R. *New J. Chem.* **2006**, *30*, 528–532.
(28) Yoshio, M.; Mukai, T.; Ohno, H.; Kato, T. *J. Am. Chem. Soc.* **2004**, *126*, 994–995.
(29) Suisse, J. M.; Bellemin-Laponnaz, S.; Douce, L.; Maisse-Francois, A.; Welter, R. *Tetrahedron Lett.* **2005**, *46*, 4303–4305.
(30) Yoshio, M.; Kagata, T.; Hoshino, K.; Mukai, T.; Ohno, H.; Kato, T. *J. Am. Chem. Soc.* **2006**, *128*, 5570–5577.
(31) Yousif, Y. Z.; Othman, A. A.; Almasoudi, W. A.; Alapati, P. R. *Liq. Cryst.* **1992**, *12*, 363–368.
(32) Cui, L.; Zhu, L. *Liq. Cryst.* **2006**, *33*, 811–818.
(33) Hoshino, K.; Yoshio, M.; Mukai, T.; Kishimoto, K.; Ohno, H.; Kato, T. *J. Polym. Sci., Part A: Polym. Chem.* **2003**, *41*, 3486–3492.
(34) Pal, S. K.; Kumar, S. *Tetrahedron Lett.* **2006**, *47*, 8993–8997.
(35) Yoshizawa, H.; Mihara, T.; Koide, N. *Mol. Cryst. Liq. Cryst.* **2004**, *423*, 61–72.
(36) Yoshizawa, H.; Mihara, T.; Koide, N. *Liq. Cryst.* **2005**, *32*, 143–149.
(37) Kumar, S.; Pal, S. K. *Tetrahedron Lett.* **2005**, *46*, 2607–2610.
(38) Bravo-Grimaldo, E.; Navarro-Rodriguez, D.; Skoulios, A.; Guillon, D. *Liq. Cryst.* **1996**, *20*, 393–398.
(39) Chovino, C.; Frere, Y.; Guillon, D.; Gramain, P. *J. Polym. Sci., Part A: Polym. Chem.* **1997**, *35*, 2569–2577.
(40) Cui, L.; Sapagovas, V.; Lattermann, G. *Liq. Cryst.* **2002**, *29*, 1121–1132.
(41) Kumar, S.; Pal, S. K. *Tetrahedron Lett.* **2005**, *46*, 4127–4130.
(42) Navarro-Rodriguez, D.; Frere, Y.; Gramain, P.; Guillon, D.; Skoulios, A. *Liq. Cryst.* **1991**, *9*, 321–335.
(43) Kato, T.; Mizoshita, N.; Kishimoto, K. *Angew. Chem., Int. Ed.* **2006**, *45*, 38–68.
(44) Yoshio, M.; Mukai, T.; Kanie, K.; Yoshizawa, M.; Ohno, H.; Kato, T. *Adv. Mater.* **2002**, *14*, 351–354.
(45) Lin, I. J. B.; Vasam, C. S. *J. Organomet. Chem.* **2005**, *690*, 3498–3512.
(46) Neve, F. *Adv. Mater.* **1996**, *8*, 277–289.
(47) Giroud-Godquin, A. M.; Maitlis, P. M. *Angew. Chem., Int. Ed.* **1991**, *30*, 375–402.
(48) Donnio, B.; Guillon, D.; Deschenaux, R.; Bruce, D. W. Metallomesogens. In *Comprehensive Coordination Chemistry II*; McCleverty, J. A., Meyer, T. J., Eds.; Elsevier: Oxford, UK, 2003; pp 357–627.
(49) *Metallomesogens, Synthesis, Properties and Applications*; Serrano, J. L., Ed.; VCH: Weinheim, Germany, 1996.
(50) Hudson, S. A.; Maitlis, P. M. *Chem. Rev.* **1993**, *93*, 861–885.
(51) Batra, D.; Seifert, S.; Varela, L. M.; Liu, A. C. Y.; Firestone, M. A. *Adv. Funct. Mater.* **2007**, *17*, 1279–1287.
(52) Dobbs, W.; Suisse, J. M.; Douce, L.; Welter, R. *Angew. Chem., Int. Ed.* **2006**, *45*, 4179–4182.
(53) Taubert, A.; Arbell, I.; Mecke, A.; Graf, P. *Gold Bull.* **2006**, *39*, 205–211.
(54) Taubert, A.; Palivan, C.; Casse, O.; Gozzo, F.; Schmitt, B. *J. Phys. Chem. C* **2007**, *111*, 4077–4082.
(55) Lee, C. K.; Vasam, C. S.; Huang, T. W.; Wang, H. M. J.; Yang, R. Y.; Lee, C. S.; Lin, I. J. B. *Organometallics* **2006**, *25*, 3768–3775.
(56) Binnemans, K.; Görller-Walrand, C. *Chem. Rev.* **2002**, *102*, 2303–2345.
(57) Binnemans, K.; Galyametdinov, Y. G.; Van Deun, R.; Bruce, D. W.; Collinson, S. R.; Polishchuk, A. P.; Bikchantaev, I.; Haase, W.; Prosvirin, A. V.; Tinchurina, L.; Litvinov, I.; Gubajdullin, A.; Rakhmatullin, A.; Uytterhoeven, K.; Van Meervelt, L. *J. Am. Chem. Soc.* **2000**, *122*, 4335–4344.
(58) Van Deun, R.; Binnemans, K. *Liq. Cryst.* **2001**, *28*, 621–627.
(59) Galyametdinov, Y. G.; Haase, W.; Malykhina, L. V.; Prosvirin, A.; Bikchantaev, I.; Rakhmatullin, A.; Binnemans, K. *Chem.—Eur. J.* **2001**, *7*, 99–105.
(60) Binnemans, K.; Lodewyckx, K. *Angew. Chem., Int. Ed.* **2001**, *40*, 242–244.
(61) Binnemans, K.; Lodewyckx, K.; Donnio, B.; Guillon, D. *Chem.—Eur. J.* **2002**, *8*, 1101–1105.
(62) Piguet, C.; Bünzli, J. C. G.; Donnio, B.; Guillon, D. *Chem. Commun.* **2006**, *3755*, 3768.
(63) Terazzi, E.; Suarez, S.; Torelli, S.; Nozary, H.; Imbert, D.; Mamula, O.; Rivera, J. P.; Guillet, E.; Benech, J. M.; Bernardinelli, G.; Scopelliti, R.; Donnio, B.; Guillon, D.; Bünzli, J. C. G.; Piguet, C. *Adv. Funct. Mater.* **2006**, *16*, 157–168.
(64) Terazzi, E.; Torelli, S.; Bernardinelli, G.; Rivera, J. P.; Benech, J. M.; Bourgogne, C.; Donnio, B.; Guillon, D.; Imbert, D.; Bünzli, J. C. G.; Pinto, A.; Jeannerat, D.; Piguet, C. *J. Am. Chem. Soc.* **2005**, *127*, 888–903.

flashlamp (pulse length: 2 μs), and a red-sensitive photomultiplier (300–850 nm). The excitation wavelength was 390 nm.

Colorless single crystals of **4a** were obtained after 3 days by slowly evaporating a solution of **4a** in chloroform. X-ray intensity data were collected on a SMART 6000 diffractometer equipped with a CCD detector using Cu Kα radiation (λ= 1.5418 Å). The images were interpreted and integrated with the program SAINT from Bruker.[65] **4a**: $C_{28}H_{36}BrN_3O$, M = 510.51 g mol^{-1}, triclinic, *P*-1 (No. 2), a = 7.2728(1) Å, b = 9.8872(1) Å, c = 17.5211(2) Å, α = 89.918(1)°, β = 87.655(1)°, γ = 85.541(1)°, V = 1255.03(3) Å^3, T = 100(2) K, Z = 2, ρ_{calc} = 1.351 g cm^{-3}, μ(Cu Kα) = 2.416 mm^{-1}, F(000) = 536, crystal size 0.4 × 0.3 × 0.15 mm^3, 4646 independent reflections (R_{int} = 0.0401). Final R = 0.0329 for 4647 reflections with $I > 2\sigma(I)$ and $\omega R2$ = 0.0817 for all data. Yellow single crystals of **8** were obtained after 1 day by evaporating a solution of **8** in ethanol/dichloromethane. **8**: $C_{54}H_{59}EuF_{12}N_2O_8S_4$, M = 1372.26 g mol^{-1}, triclinic, *P*-1 (No. 2), a = 10.7453(6) Å, b = 12.3222(6) Å, c = 23.4432(1) Å, α = 87.275(3)°, β = 80.608(4)°, γ = 71.755(4)°, V = 2908.4(3) Å^3, T = 100(2) K, Z = 2, ρ_{calc} = 1.567 g cm^{-3}, μ(Cu Kα) = 9.870 mm^{-1}, F(000) = 1392, crystal size 0.5 × 0.2 × 0.15 mm^3, 11056 independent reflections (R_{int} = 0.0957). Final R = 0.0475 for 9792 reflections with $I > 2\sigma(I)$ and $\omega R2$ = 0.1179 for all data. The structures were solved by direct methods and refined by full-matrix least-squares on F^2 using the SHELXTL program package.[66] Non-hydrogen atoms were anisotropically refined and the hydrogen atoms in the riding mode with isotropic temperature factors fixed at 1.2 times U(eq) of the parent atoms (1.5 times for methyl groups). CCDC-634819 and CCDC-665178 contain the supplementary crystallographic data for this paper and can be obtained free of charge via www.ccdc.cam.ac.uk/conts/retrieving.html (or from the Cambridge Crystallographic Data Centre, 12, Union Road, Cambridge CB2 1EZ, UK; fax +44-1223-336033; or deposit@ccdc.cam.ac.uk).

Synthetic Procedures. The synthesis of the precursors **1**–**3**, europium(III) triflate, and **8** is described in the Supporting Information.

*Synthesis of **4a** (1).* A solution of **1** (11.00 mmol, 4.713 g) in dry toluene was added dropwise to a solution of 1-methylimidazole (10.00 mmol, 0.80 mL, freshly distilled over KOH) in dry toluene, and the mixture was stirred for 24 h at 100 °C under an argon atmosphere. A white precipitate was formed, filtered off, washed with diethyl ether, and dried in vacuo at 50 °C. Yield: 81% (4.15 g). δ_H (300 MHz, $CDCl_3$): 1.24–1.70 (m, 14H, CH_2), 1.74–1.86 (m, 2H, C**H**$_2$–CH_2–O), 1.86–1.98 (m, 2H, N–CH_2–C**H**$_2$), 4.00 (t, 2H, CH_2–O), 4.13 (s, 3H, N–CH_3), 4.32 (t, 2H, N–CH_2), 6.99 (d, 2H, H–aryl, J_o = 8.7 Hz), 7.24 (s, 1H, N–C**H**=CH–N), 7.31 (s, 1H, N–CH=C**H**–N), 7.52 (d, 2H, H–aryl, J_o = 8.7 Hz), 7.61–7.71 (m, 4H, H–aryl), 10.73 (s, 1H, N=CH–N). δ_C (75 MHz, $CDCl_3$): 26.11, 26.35, 29.06, 29.30, 29.43, 29.49, 29.55, 30.40, 36.88, 50.32, 68.24, 110.06, 115.18, 119.23, 121.72, 123.38, 127.16, 128.41, 131.30, 132.66, 138.00, 145.37, 159.89. Calcd for $C_{28}H_{36}BrN_3O$ (510.51): C 65.88, H 7.11, N 8.23. Found: C 65.98, H 7.37, N 8.11. ESI-MS (methanol, *m*/*z*): 430.5, [M – Br$^-$]$^+$; 941.2, [M + M – Br$^-$]$^+$.

*Synthesis of **4b** (2).* An aqueous solution of **4a** (0.28 mmol, 0.143 g) was heated to 50 °C, after which an aqueous solution of $LiNTf_2$ (0.34 mmol, 0.097 g) was added dropwise. Then the reaction mixture was stirred for 3 h at 50 °C. A white precipitate was formed, filtered off, washed with water, and dried in vacuo at 50 °C. Yield: 76% (0.15 g). δ_H (300 MHz, $CDCl_3$): 1.15–1.60 (m, 16H, CH_2), 1.74–1.90 (m, 2H, N–CH_2–C**H**$_2$), 3.95 (s, 3H, N–CH_3), 4.00 (t, 2H, CH_2–O), 4.16 (t, 2H, N–CH_2), 6.98 (d, 2H, H–aryl, J_o = 8.5 Hz), 7.26 (s, 1H, N–C**H**=CH–N), 7.28 (s, 1H, N–CH=C**H**–N), 7.52 (d, 2H, H–aryl, J_o = 8.5 Hz), 7.61–7.70 (m, 4H, H–aryl), 8.79 (s, 1H, N=CH–N). δ_C (75 MHz, $CDCl_3$): 26.12, 26.23, 28.96, 29.36, 29.43, 29.58, 30.19, 36.55, 50.41, 68.29, 110.09, 115.21, 117.80, 119.29, 122.06, 122.19, 123.68, 127.18, 128.45, 131.35, 132.69, 136.41, 145.42, 159.93. Calcd for $C_{30}H_{36}F_6N_4O_5S_2$ (710.75): C 50.70, H 5.11, N 7.88. Found: C 50.72, H 5.28, N 7.73. ESI-MS (methanol, *m*/*z*): 430.5, [M – NTf_2^-]$^+$; 1140.1, [M + M – NTf_2^-]$^+$.

*Synthesis of **4c** (3).* **4a** (1.00 mmol, 0.511 g), 2-thenoyltrifluoroacetone (4.00 mmol, 0.89 g), and NaOH (4.00 mmol, 1 mol L^{-1} aqueous solution) were added to 15 mL of ethanol. The mixture was heated to 50 °C and stirred until a clear solution was formed. A solution of europium(III) triflate (0.95 mmol, 0.569 g) in 3 mL of water was added dropwise, and the mixture was stirred for 1.5 h at 50 °C. A yellow precipitate was formed, filtered off, and washed with ice-cold water. The crude product was recrystallized from EtOH/CH_2Cl_2 and dried in vacuo at 50 °C. Yield: 79% (1.10 g). Calcd for $C_{60}H_{52}EuF_{12}N_3O_9S_4$ (1467.27): C 49.11, H 3.57, N 2.86. Found: C 48.98, H 4.06, N 2.64. ESI-MS (methanol, *m*/*z*): 430.2, [M – [Eu(tta)$_4$]$^-$]$^+$; 1898.6, [M + M – [Eu(tta)$_4$]$^-$]$^+$; 1036.7, [Eu(tta)$_4$]$^-$ (observed in negative mode).

*Synthesis of **5a** (4).* A solution of **3** (3.44 mmol, 2.132 g) in dry toluene was added dropwise to a solution of 1-methylimidazole (3.13 mmol, 0.25 mL, freshly distilled over KOH) in dry toluene, and the mixture was stirred for 48 h at 100 °C under an argon atmosphere. The solvent was removed under reduced pressure, and the crude product was purified on a silica column with $CHCl_3$/MeOH (90:10) as the eluent (TLC spots were visualized by iodine vapor). The pure compound was obtained as a white-gray product and dried in vacuo at 50 °C for a few days. Yield: 69% (1.52 g). δ_H (400 MHz, DMSO-d_6): 0.65 (s, 3H, CH_3), 0.82–1.58 (m, 49H), 1.72–2.10 (m, 8H), 2.24–2.34 (m, 1H), 2.99–3.09 (m, 1H, $(CH_2)_2$C**H**–O), 3.36 (t, 2H, CH_2–O), 3.85 (s, 3H, N–CH_3), 4.14 (t, 2H, N–CH_2), 5.30 (s, 1H, CH=CR_2), 7.69 (s, 1H, N–C**H**=CH–N), 7.76 (s, 1H, N–CH=C**H**–N), 9.12 (s, 1H, N=CH–N). δ_C (100 MHz, DMSO-d_6): 11.61, 18.49, 19.00, 20.55, 22.31, 22.57, 23.14, 23.79, 25.42, 25.67, 27.30, 27.69, 28.09, 28.28, 28.71, 28.81, 28.90, 29.29, 29.63, 31.30, 31.37, 35.11, 35.60, 35.68, 36.26, 36.67, 38.79, 41.80, 48.71, 49.59, 55.56, 56.14, 67.01, 78.05, 120.89, 122.20, 123.53, 136.43, 140.56. Calcd for $C_{42}H_{73}BrN_2O \cdot 1.5H_2O$ (728.98): C 69.20, H 10.51, N 3.84. Found: C 69.53, H 10.57, N 3.84. ESI-MS (methanol, *m*/*z*): 621.9, [M – Br$^-$]$^+$; 1323.7, [M + M – Br$^-$]$^+$.

*Synthesis of **5b** (5).* **5a** (0.22 mmol, 0.162 g) was dissolved in water at 60 °C, and ethanol was added until a clear solution was formed. Then an aqueous solution of $LiNTf_2$ (0.27 mmol, 0.076 g) was added dropwise, and the reaction mixture was stirred for 3 h at 60 °C. A white precipitate was formed, filtered off, washed with water, and dried in vacuo at 50 °C. Yield: 75% (0.15 g). δ_H (300 MHz, $CDCl_3$): 0.67 (s, 3H, CH_3), 0.83–2.39 (m, 58 H), 3.06–3.18 (m, 1H, $(CH_2)_2$C**H**–O), 3.44 (t, 2H, CH_2–O), 3.96 (s, 3H, N–CH_3), 4.17 (t, 2H, N–CH_2), 5.34 (d, 1H, CH=CR_2, J = 4.8 Hz), 7.26 (s, 1H, N–C**H**=CH–N), 7.29 (s, 1H, N–CH=C**H**–N), 8.87 (s, 1H, N=CH–N). δ_C (75 MHz, $CDCl_3$): 11.99, 18.86, 19.53, 21.21, 22.71, 22.96, 23.96, 24.44, 26.28, 26.34, 28.16, 28.38, 28.65, 28.99, 29.41, 29.54, 29.62, 30.21, 30.38, 32.04, 32.09, 35.93, 36.33, 36.60, 37.06, 37.44, 39.37, 39.65, 39.93, 42.45, 50.35, 50.44, 56.31, 56.92, 68.29, 79.10, 121.56, 122.05, 122.14, 123.66, 136.58, 141.30. Calcd for $C_{44}H_{73}F_6N_3O_5S_2$ (902.19): C 58.58, H 8.16, N 4.66. Found: C 59.06, H 7.97, N 4.64. ESI-MS (methanol, *m*/*z*): 621.9, [M – NTf_2^-]$^+$; 1522.5, [M + M – NTf_2^-]$^+$.

*Synthesis of **5c** (6).* **5a** (0.15 mmol, 0.109 g), 2-thenoyltrifluoroacetone (0.60 mmol, 0.133 g), and NaOH (0.60 mmol, 1 mol L^{-1}

(65) *SAINT*,version 5/6.0; Bruker Analytical X-ray Systems Inc.: Madison, WI, 1997.

(66) *SHELXTL-PC*,version 5.1; Bruker Analytical X-ray Systems Inc.: Madison, WI, 1997.

aqueous solution) were added to 10 mL of ethanol. The mixture was heated to 55 °C and stirred until a clear solution was formed. A solution of europium(III) triflate (0.14 mmol, 0.085 g) in 2 mL of water was added dropwise, and the mixture was stirred for 1.5 h at 55 °C. A yellow precipitate was formed, filtered off, and washed with ice-cold water. The crude product was dissolved in chloroform, and the solution was filtered. The pure compound was precipitated from the filtrate by adding hexane. The precipitate was filtered off and dried in vacuo at 50 °C. Yield: 23% (0.05 g). Calcd for $C_{74}H_{89}EuF_{12}N_2O_9S_4$ (1658.71): C 53.58, H 5.41, N 1.69. Found: C 53.32, H 5.29, N 1.75. ESI-MS (methanol, *m*/*z*): 621.6, $[M - [Eu(tta)_4]^-]^+$; 2279.9, $[M + M - [Eu(tta)_4]^-]^+$; 1036.7, $[Eu(tta)_4]^-$ (observed in negative mode).

*Synthesis of **6a** (7).* A solution of imidazole (3.38 mmol, 0.230 g) in dry THF was added dropwise to an ice-cooled stirred solution of NaH (3.55 mmol, 0.142 g of a 60% dispersion in mineral oil) in dry THF. The mixture was stirred for 1 h at room temperature and for 1 h at 55 °C under an argon atmosphere. (The formation of hydrogen gas could be observed by the formation of bubbles in the solution.) Then a solution of **1** (7.43 mmol, 3.182 g) in dry THF was added dropwise, and the mixture was refluxed for 48 h under an argon atmosphere. The white precipitate (NaBr) was filtered off and washed with chloroform. The solvent was removed under reduced pressure, and the resulting product was dissolved in chloroform and washed with water. The organic layer was dried over $MgSO_4$, and the solvent was removed under reduced pressure. The crude product was purified on an alumina column with $CHCl_3$/MeOH (95:5) as the eluent. The product was dissolved in EtOH/$CHCl_3$ and precipitated by adding hexane. The white precipitate was filtered off and dried in vacuo at 50 °C. Yield: 59% (1.68 g). δ_H (300 MHz, $CDCl_3$): 1.23–1.72 (m, 28H, CH_2), 1.74–1.85 (m, 4H, C**H**$_2$–CH_2–O), 1.86–1.98 (m, 4H, N–CH_2–C**H**$_2$), 4.00 (t, 4H, CH_2–O), 4.35 (t, 4H, N-CH_2), 6.98 (d, 4H, H–aryl, J_o = 8.7 Hz), 7.16 (s, 2H, N–C**H**=CH–N), 7.52 (d, 4H, H–aryl, J_o = 8.7 Hz), 7.61–7.71 (m, 8H, H–aryl), 11.23 (s, 1H, N=CH–N). δ_C (75 MHz, $CDCl_3$): 26.49, 26.74, 26.94, 29.47, 29.68, 29.82, 29.87, 29.94, 30.81, 50.59, 68.62, 79.89, 110.43, 115.56, 115.69, 119.62, 121.92, 122.02, 127.53, 127.62, 127.71, 128.78, 131.65, 133.02, 138.88, 145.74, 160.27. Calcd for $C_{51}H_{63}BrN_4O_2 \cdot H_2O$ (861.99): C 71.06, H 7.60, N 6.50. Found: C 71.45, H 7.21, N 6.35. ESI-MS (methanol, *m*/*z*): 763.8, $[M - Br^-]^+$.

*Synthesis of **6b** (8).* **6a** (0.19 mmol, 0.165 g) was dissolved in water at 75 °C, and ethanol was added until a clear solution was formed. An aqueous solution of $LiNTf_2$ (0.23 mmol, 0.066 g) was added dropwise, and the reaction mixture was stirred for 3 h at 75 °C. A white precipitate was formed, filtered off, washed with water, and dried in vacuo at 50 °C. Yield: 64% (0.13 g). δ_H (300 MHz, $CDCl_3$): 1.22–1.58 (m, 32H, CH_2), 1.73–1.91 (m, 4H, N–CH_2–C**H**$_2$), 3.99 (t, 4H, CH_2–O), 4.19 (t, 4H, N-CH_2), 6.97 (d, 4H, H–aryl, J_o = 8.5 Hz), 7.24 (s, 1H, N–C**H**=CH–N), 7.26 (s, 1H, N–CH=C**H**–N), 7.51 (d, 4H, H–aryl, J_o = 8.5 Hz), 7.60–7.70 (m, 8H, H–aryl), 8.97 (s, 1H, N=CH–N). δ_C (75 MHz, $CDCl_3$): 26.14, 26.26, 28.97, 29.34, 29.41, 29.46, 29.58, 30.28, 50.45, 68.27, 110.12, 115.21, 117.83, 119.26, 122.03, 127.19, 128.46, 131.35, 132.70, 136.24, 145.40, 159.93. Calcd for $C_{53}H_{63}F_6N_5O_6S_2$ (1044.22): C 60.96, H 6.08, N 6.71. Found: C 61.14, H 5.86, N 6.57. ESI-MS (methanol, *m*/*z*): 763.9, $[M - NTf_2^-]^+$; 1807.3, $[M + M - NTf_2^-]^+$.

*Synthesis of **6c** (9).* **6a** (0.14 mmol, 0.119 g), 2-thenoyltrifluoroacetone (0.55 mmol, 0.122 g), and NaOH (0.55 mmol, 1 mol L^{-1} aqueous solution) were added to 10 mL of ethanol. The mixture was heated to 60 °C and stirred until a clear solution was formed. A solution of europium(III) triflate (0.13 mmol, 0.078 g) in 2 mL of water was added dropwise, and the mixture was stirred for 1.5 h at 60 °C. A yellow precipitate was formed, filtered off, washed with ice-cold water, and dried in vacuo at 50 °C. Yield: 64% (0.15 g). Calcd for $C_{83}H_{79}EuF_{12}N_4O_{10}S_4$ (1800.74): C 55.36, H 4.42, N 3.11. Found: C 55.77, H 4.38, N 3.07. ESI-MS (methanol, *m*/*z*): 763.6, $[M - [Eu(tta)_4]^-]^+$; 2564.9, $[M + M - [Eu(tta)_4]^-]^+$; 1036.9, $[Eu(tta)_4]^-$ (observed in negative mode).

*Synthesis of **7a** (10).* A solution of imidazole (2.06 mmol, 0.140 g) in dry THF was added dropwise to an ice-cooled stirred solution of NaH (2.17 mmol, 0.087 g of a 60% dispersion in mineral oil) in dry THF. The mixture was stirred for 1 h at room temperature and for 1 h at 55 °C under an argon atmosphere. (The formation of hydrogen gas could be observed by the formation of bubbles in the solution.) Then a solution of bromide **3** (4.54 mmol, 2.814 g) in dry THF was added dropwise, and the mixture was refluxed for 96 h under an argon atmosphere. The white precipitate (NaBr) was filtered off and washed with chloroform. The solvent was removed under reduced pressure, and the resulting product was dissolved in chloroform and washed with water. The organic layer was dried over $MgSO_4$, and the solvent was removed under reduced pressure. The crude product was purified on a silica column with $CHCl_3$/MeOH (94:6) as the eluent (TLC spots were visualized by iodine vapor). The white product was recrystallized from EtOH/$CHCl_3$ and dried in vacuo at 50 °C. Yield: 29% (0.73 g). δ_H (300 MHz, $CDCl_3$): 0.67 (s, 6H, CH_3), 0.82–2.39 (m, 116H), 3.06–3.17 (m, 2H, $(CH_2)_2$C**H**–O), 3.44 (t, 4H, CH_2–O), 4.35 (t, 4H, N–CH_2), 5.33 (d, 2H, CH=CR_2, J = 4.8 Hz), 7.17 (s, 2H, N–C**H**=C**H**–N), 10.97 (s, 1H, N=CH–N). δ_C (75 MHz, $CDCl_3$): 12.02, 18.88, 19.54, 21.25, 22.70, 22.94, 24.00, 24.46, 26.37, 26.40, 28.16, 28.38, 28.70, 29.09, 29.46, 29.54, 29.60, 29.63, 30.40, 30.43, 32.11, 35.94, 36.38, 37.09, 37.50, 39.43, 39.69, 40.00, 42.52, 50.43, 56.38, 56.99, 68.30, 79.13, 121.33, 121.54, 138.56, 141.37. Calcd for $C_{79}H_{137}BrN_2O_2 \cdot H_2O$ (1244.86): C 76.22, H 11.25, N 2.25. Found: C 76.31, H 11.14, N 2.23. ESI-MS (methanol, *m*/*z*): 1146.7, $[M - Br^-]^+$.

*Synthesis of **7b** (11).* **7a** (0.08 mmol, 0.105 g) was dissolved in water at 75 °C, and ethanol was added until a clear solution was formed. An aqueous solution of $LiNTf_2$ (0.10 mmol, 0.029 g) was added dropwise, and the reaction mixture was stirred for 3 h at 75 °C. A white precipitate was formed, filtered off, washed with water, and dried in vacuo at 50 °C. Yield: 20% (0.02 g). δ_H (300 MHz, $CDCl_3$): 0.67 (s, 6H, CH_3), 0.83–2.40 (m, 116H), 3.06–3.17 (m, 2H, $(CH_2)_2$C**H**–O), 3.44 (t, 4H, CH_2–O), 4.23 (t, 4H, N–CH_2), 5.34 (s, 2H, CH=CR_2), 7.20 (s, 2H, N–C**H**=C **H**–N), 9.20 (s, 1H, N=CH–N). Calcd for $C_{81}H_{137}F_6N_3O_6S_2$ (1427.09): C 68.17, H 9.68, N 2.94. Found: C 68.44, H 9.33, N 2.92. ESI-MS (methanol, *m*/*z*): 1146.5, $[M - NTf_2^-]^+$.

*Synthesis of **7c** (12).* **7a** (0.09 mmol, 0.107 g), 2-thenoyltrifluoroacetone (0.35 mmol, 0.078 g), and NaOH (0.350 mmol, 1 mol L^{-1} aqueous solution) were added to 10 mL of ethanol. The mixture was heated to 65 °C and stirred until a clear solution was formed. A solution of europium(III) triflate (0.08 mmol, 0.050 g) in 2 mL of water was added dropwise, and the mixture was stirred for 1.5 h at 65 °C. A yellow precipitate was formed, filtered off, washed with ice-cold water, and dried in vacuo at 50 °C. Yield: 40% (0.07 g). Calcd for $C_{111}H_{153}EuF_{12}N_2O_{10}S_4$ (2183.61): C 61.05, H 7.06, N 1.28. Found: C 61.44, H 6.98, N 1.43. ESI-MS (methanol, *m*/*z*): 1146.1, $[M - [Eu(tta)_4]^-]^+$; 3330.9, $[M + M - [Eu(tta)_4]^-]^+$; 1036.9, $[Eu(tta)_4]^-$ (observed in negative mode).

Results and Discussion

Synthesis. The synthesis of the precursors is outlined in Scheme 1. 4′-Hydroxy-4-biphenylcarbonitrile and 11-bromoundecanol were coupled via the hydroxyl group by a

Scheme 1. Synthesis of the Precursors[a]

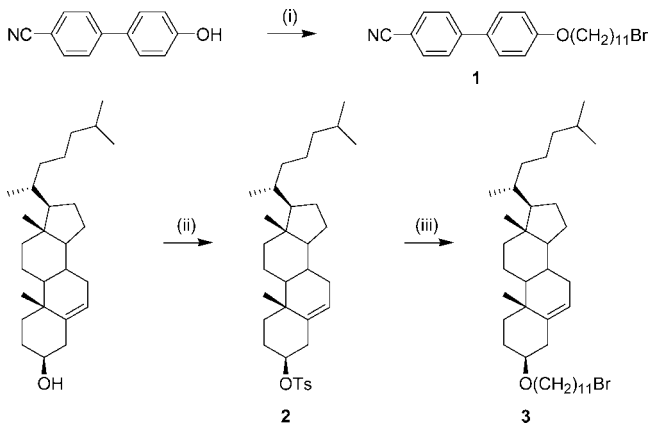

[a] (i) 11-Bromo-1-undecanol, PPh_3, DIAD, THF, rt; (ii) *p*-toluenesulfonyl chloride, pyridine, rt; (iii) 11-bromo-1-undecanol, 1,4-dioxane, reflux.

Mitsunobu reaction to give the precursor **1**.[67] For the Mitsunobu reaction, diisopropyl azodicarboxylate (DIAD) was preferred to diethyl azodicarboxylate (DEAD) as the reagent because DIAD is more convenient and safer to use. Precursor **3** was prepared following literature procedures.[68,69] Initially, cholesterol was converted to cholest-5-en-3β-tosylate (**2**), which was coupled with 11-bromo-1-undecanol in a second reaction step to give **3**.

The synthesis of the 3-monosubstituted imidazolium compounds and the 1,3-disubstituted imidazolium compounds is outlined in Schemes 2 and 3, respectively. The 3-monosubstituted 1-methylimidazolium compounds **4a** and **5a** were prepared by the quaternization of 1-methylimidazole with **1** and **3**, respectively. The 1,3-disubstituted imidazolium compounds **6a** and **7a** were prepared in a single reaction step between imidazole, sodium hydride, and **1** and **3**, respectively.[70] The bis(trifluoromethylsulfonyl)imide salts **4b–7b** were synthesized from the bromide salts **4a–7a** by a metathesis reaction between lithium bis(trifluoromethylsulfonyl)imide ($LiNTf_2$, Tf = SO_2CF_3) and **4a–7a**, respectively.[21] The tetrakis(2-thenoyltrifluoroacetonato)europate(III) salts **4c–7c** were prepared by a reaction between the bromide salts **4a–7a**, 2-thenoyltrifluoroacetone (Htta), sodium hydroxide, and europium(III) triflate.[71]

In the crystal structure of **4a**, each of the two bromide anions are linked through hydrogen bonds (ranging from 2.83 to 3.00 Å) to the acidic H(C2) and H(C3) hydrogen atoms of the imidazolium cations, resulting in the formation of *trans*-dimeric units (Figure 1). Each bromide anion is almost basal with respect to the closest imidazolium cation and apical with respect to the other imidazolium cation. The Br1–H(C2)–C2–C3 dihedral angle is 13.99°, and the Br1–H(C3)–C3–C2 dihedral angle is 57.82°. Intermolecular short ring–ring interactions are observed for the imidazolium cation and one phenyl ring of the cyanobiphenyl unit. The shortest distance between these centroids is 3.77 Å.

Unfortunately, it was not possible to obtain single crystals of the tetrakis(2-thenoyltrifluoroacetonato)europate(III) salts **4c–7c**. Therefore, the analogous $[C_{18}mim][Eu(tta)_4]$ complex (**8**) (which contains one long octadecyl chain) was prepared (see Supporting Information) in order to obtain more information about the structure of this type of complex. The crystal structure of **8** (Figure 2, top) consists of $[C_{18}mim]^+$ cations and $[Eu(tta)_4]^-$ anions. The europium(III) ion is surrounded by four 2-thenoyltrifluoroacetonate (tta^-) ligands. The coordination number of the europium(III) ion is eight, and the coordination polyhedron can be described as a distorted square antiprism. Each of the acidic H(C2), H(C4), and H(C5) hydrogens of the imidazolium cations form strong hydrogen bonds with the oxygen atoms of each two adjacent $[Eu(tta)_4]^-$ moieties with H···O distances in a range from 2.29 to 2.58 Å (Figure 2, bottom). In the packing of the crystal structure, double layers of the anions parallel to the [110] direction are alternating with double layers of the cations (see Supporting Information).

Luminescence Properties. The photoluminescence of **7c** was studied. The luminescence spectra were recorded at room temperature (18 °C) on a polycrystalline powder sample as well as on a vitrified mesophase sample. This vitrified mesophase sample was obtained by heating the compound between two quartz plates to the isotropic liquid, followed by cooling of the sample into the mesophase, whereafter it was supercooled using liquid nitrogen. The sample was checked by polarizing optical microscopy (POM) (before and after recording the luminescence spectra) to verify that the mesomorphic order was frozen at room temperature and that there were no crystalline domains present in the sample. The monodomains in the vitrified mesophase were randomly oriented. The luminescence spectra look similar, but the powder sample shows narrower emission lines and more pronounced crystal-field splitting (Figure 3). The luminescent europium(III) ion is a sensitive probe for the rare-earth site symmetry, since differences in site symmetry result in differences in relative intensities and fine structure in the spectra.[72] The luminescence transitions start from the nondegenerate excited $^5D_0$ state, which makes the interpretation of the spectra less complicated. The luminescence spectra of the two samples are dominated by the $^5D_0 \rightarrow {}^7F_2$ line. This forced electric dipole transition is much more intense than the magnetic dipole transition $^5D_0 \rightarrow {}^7F_1$. The integrated intensity ratio of the $^5D_0 \rightarrow {}^7F_2$ line to that of the $^5D_0 \rightarrow {}^7F_1$line, $I(^5D_0 \rightarrow {}^7F_2)/I(^5D_0 \rightarrow {}^7F_1)$, is 15.7 for the powder and 17.8 for the vitrified mesophase. An intense $^5D_0 \rightarrow {}^7F_2$ line and an $I(^5D_0 \rightarrow {}^7F_2)/I(^5D_0 \rightarrow {}^7F_1)$ ratio of about 16 are typical for europium(III) β-diketonate complexes.[73] The other transitions to the ^7F_J levels have a weak intensity and do not contribute appreciably to the luminescence output. The $^5D_0 \rightarrow {}^7F_0$ line is very weak in the vitrified mesophase sample but can hardly be observed in the powder sample. The

(67) Mitsunobu, O. *Synthesis* **1981**, 1–28.
(68) Davis, S. C.; Szoka, F. C. *Bioconjugate Chem.* **1998**, *9*, 783–792.
(69) Krishnan-Ghosh, Y.; Gopalan, R. S.; Kulkarni, G. U.; Bhattacharya, S. *J. Mol. Struct.* **2001**, *560*, 345–355.
(70) Dzyuba, S. V.; Bartsch, R. A. *Chem. Commun.* **2001**, 1466–1467.
(71) Nockemann, P.; Beurer, E.; Driesen, K.; Van Deun, R.; Van Hecke, K.; Van Meervelt, L.; Binnemans, K. *Chem. Commun.* **2005**, 4354–4356.
(72) Bünzli, J. C. G.; Piguet, C. *Chem. Soc. Rev.* **2005**, *34*, 1048–1077.
(73) Binnemans, K. Rare-Earth Beta-Diketonates. In *Handbook on the Physics and Chemistry of Rare Earths*; Gschneidner, K. A., Bünzli, J. C. G., Pecharsky, V. K., Eds.; Elsevier: Amsterdam, The Netherlands, 2005; pp 107–272.

Scheme 2. Synthesis of the 3-Monosubstituted Imidazolium Compounds[a]

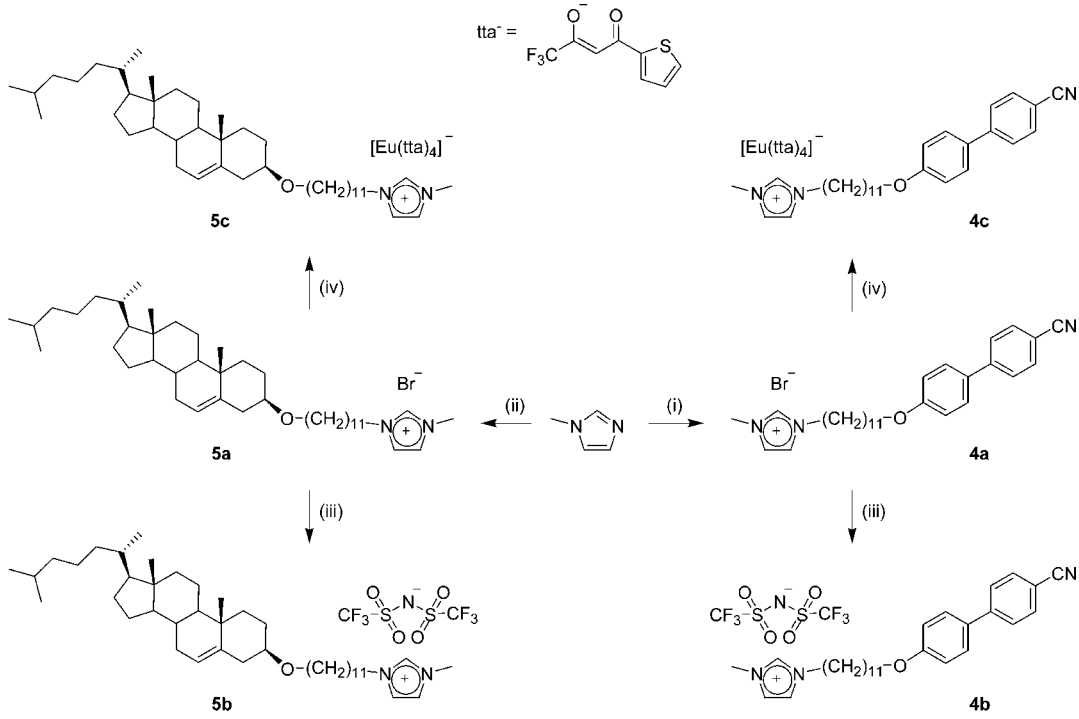

[a] (i) **1**, toluene, 100 °C; (ii) **3**, toluene, 100 °C; (iii) $LiNTf_2$, H_2O or H_2O/EtOH, 50–60 °C; (iv) 2-thenoyltrifluoroacetone, NaOH, $Eu(OTf)_3$, H_2O/EtOH, 50–55 °C.

Scheme 3. Synthesis of the 1,3-Disubstituted Imidazolium Compounds[a]

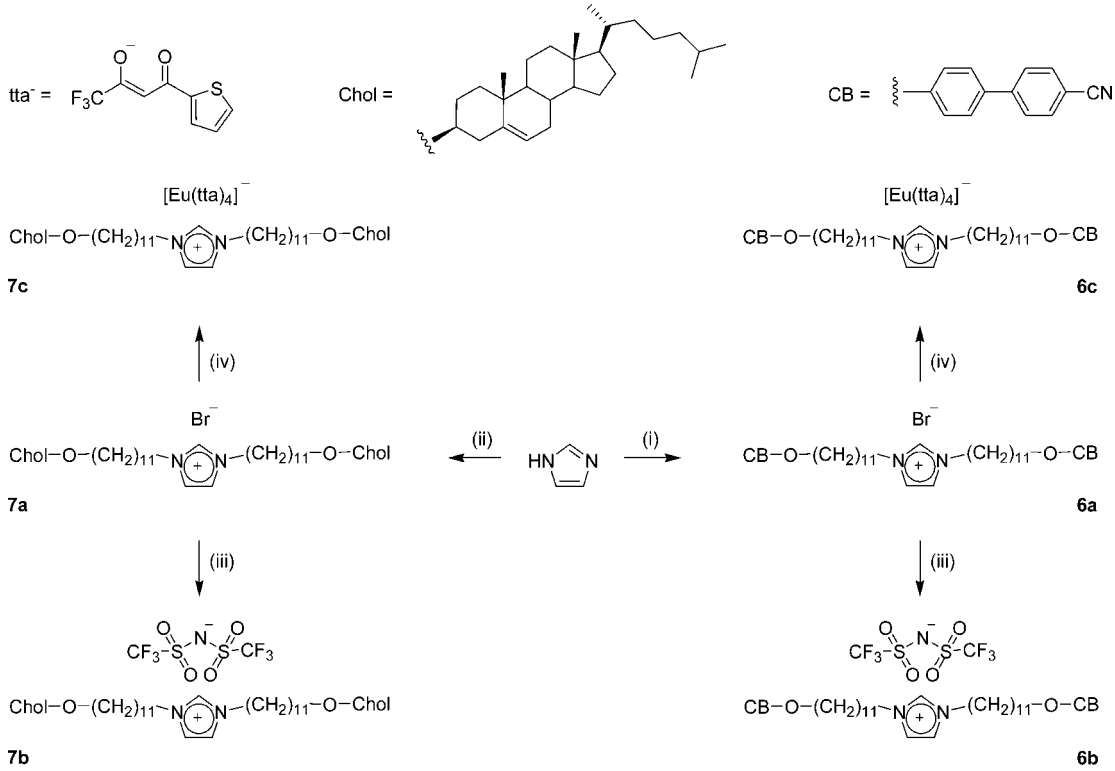

[a] (i) **1**, NaH, THF, reflux; (ii) **3**, NaH, THF, reflux; (iii) $LiNTf_2$, H_2O/EtOH, 75 °C; (iv) 2-thenoyltrifluoroacetone, NaOH, $Eu(OTf)_3$, H_2O/EtOH, 60–65 °C.

crystal-field fine structure of the $^5D_0 \rightarrow {}^7F_2$ line is not resolved in the vitreous mesophase sample, but this line is split into two sublines of roughly equal intensity in the powder sample. As can be expected, the $^5D_0 \rightarrow {}^7F_2$ line is broadened in the vitrified mesophase sample in comparison to the powder sample. The luminescence decay time of the $^5D_0$ level is 0.58 ms for the powder sample and slightly lower (0.51 ms) for the vitrified mesophase sample. The decay

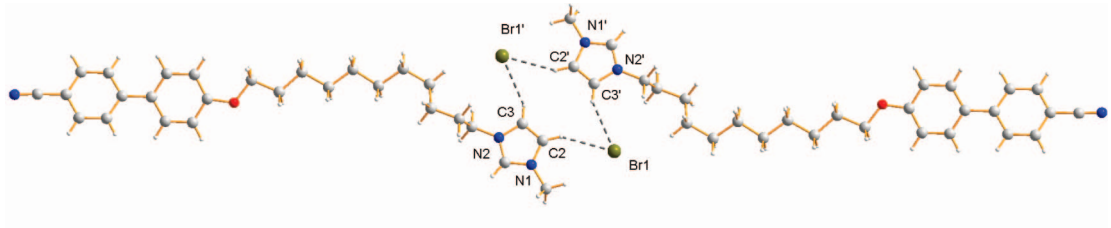

Figure 1. Hydrogen bonds in the crystal structure of **4a**, resulting in the formation of *trans*-dimeric units.

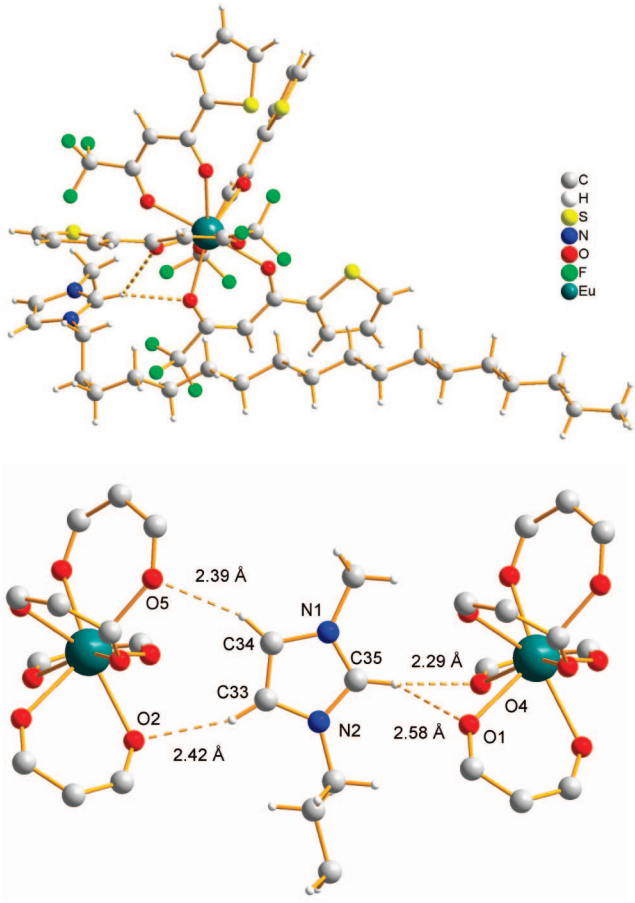

Figure 2. Top: crystal structure of **8** showing the strong hydrogen bonding between cation and anion. Bottom: cutout from the crystal structure of **8** showing the strong hydrogen bonding between cation and anion. The ligand molecules and the chain were simplified for clarity.

curves were found to be monoexponential. No important changes are observed in the luminescence spectra, and it can be concluded that during the phase transition the first coordination sphere around the europium(III) ion and therefore the coordination of the ligands to the central ion remains similar.

Thermal Behavior. The thermal properties of all the compounds were examined by polarizing optical microscopy (POM), differential scanning calorimetry (DSC), and for some of them by X-ray diffraction on powder samples (see below). The transition temperatures and thermal data for all the imidazolium salts are collected in Table 1. A typical DSC trace of **6b** is shown in Figure 4. The imidazolium salts containing one 4-cyanobiphenyl group (**4a–c**) showed a monotropic SmA phase (**4a** and **4b**) or were not liquid crystalline (**4c**). The imidazolium salts containing two 4-cyanobiphenyl groups (**6a–c**) exhibited a monotropic

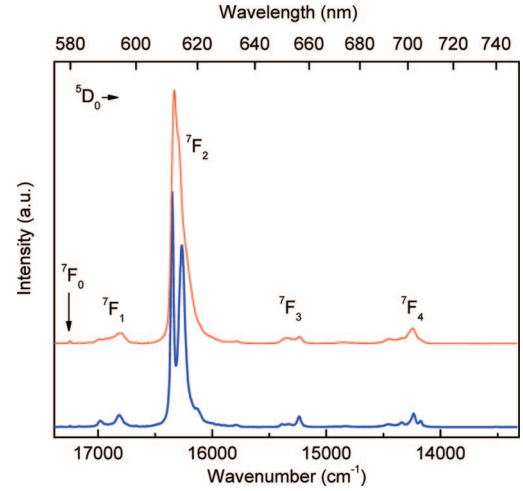

Figure 3. Room temperature luminescence spectra of **7c** in the form of a powder (blue line) and of a vitrified mesophase (red line). The excitation wavelength is 390 nm. All transitions start from the $^5D_0$ level.

Table 1. Transition Temperatures and Thermal Data for the Imidazolium Salts

compound	transition[a]	T/°C[b]	ΔH/kJ mol^{-1}	ΔS/J K^{-1} mol^{-1}
4a	(I → SmA)	96	–[c]	–[c]
	Cr → I	154	77.6	182
4b	(I → SmA)	18	11.5	40
	Cr → I	53	90.3	277
4c	Cr → I	114	99.3	257
5a	SmA* → I	180	–[c]	–[c]
5b	SmA* → I	199	–[c]	–[c]
5c	Cr → I	113	89.8	233
6a	(I → N)	100	7.8	21
	Cr → I	112	109.3	284
6b	(N → SmA)	31	3.3	11
	(I → N)	47	6.7	21
	Cr → I	62	138.9	415
6c	Cr → I	63	–[c]	–[c]
7a	Cr → SmA*	127	57.2	143
	SmA* → I	226	11.4	23
7b	Cr → SmA*	56	26.4	80
	SmA* → I	194	2.4	5
7c	(I → SmA*)	101	4.7	13
	Cr → I	121	85.0	216

[a] Abbreviations: Cr = crystalline or partially crystalline phase; SmA = smectic A phase; SmA* = chiral smectic A phase; N = nematic phase; I = isotropic liquid. [b] All the transition temperatures listed in this table are those observed by POM. [c] Not detected by DSC.

nematic phase (**6a** and **6b**) or were not liquid crystalline (**6c**). For **6b**, an additional monotropic SmA phase below the nematic phase could be observed. Although **6c** is not mesomorphic, it does present an example of a lanthanide-containing ionic liquid. Except for **5c**, which was not mesomorphic, the imidazolium salts containing one cholesterol group (**5a–c**) exhibited an enantiotropic SmA* phase over a very broad temperature range. The compounds **5a** and **5b** were liquid crystalline at room temperature, and the

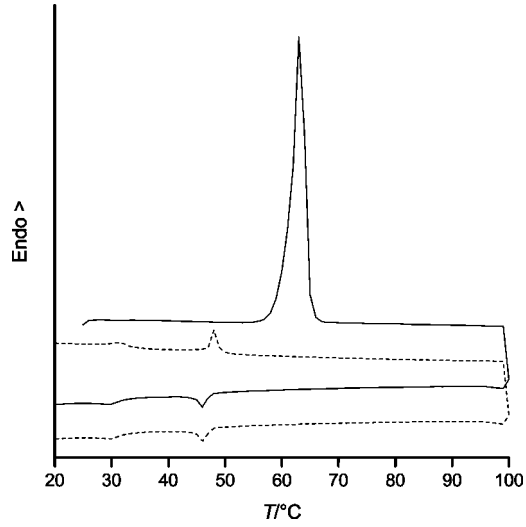

Figure 4. DSC trace of **6b** (heating/cooling rate of 10 °C min^{-1}). The first heating/cooling cycle is shown by the solid line; the second heating/cooling cycle is shown by the dashed line.

most stable mesophase was observed for **5b**. All the imidazolium salts containing two cholesterol groups (**7a–c**) exhibited a SmA* phase, which was enantiotropic for **7a** and **7b** and monotropic for **7c**. Again, the most stable mesophase was found for the bis(trifluoromethylsulfonyl)-imide salt (**7b**). The notation SmA* is used for the mesophases of the compounds containing (chiral) cholesterol moieties. The symmetry of the SmA phase is $D_{\infty h}$, which is reduced when the constituent molecules are chiral (because there can be no mirror plane). Therefore, the SmA phase composed of the cholesterol derived compounds should be designated as SmA*, although no evidence for a superstructural chirality was observed.

All the mesophases were identified by their optical textures, observed by polarizing optical microscopy. The SmA/SmA* phase was recognized by the formation of bâtonnets on cooling from the isotropic liquid. On further cooling, an oily streak texture (see Supporting Information), a focal conic texture (see Supporting Information), or a fan texture (Figure 5, top) was formed, together with large homeotropic areas. For the monotropic SmA phase of **6b**, a polygonal texture was observed (Figure 5, bottom). For the nematic phase, a Schlieren texture with two and four brushes (see Supporting Information) or a threadlike texture (Figure 6) was observed. The presence of homeotropic areas confirmed that the phase was uniaxial.

X-ray Diffraction. All the compounds showing an enantiotropic mesophase were studied by X-ray diffraction on powder samples (except for **7b**, which was unfortunately obtained in too low quantity for further analysis). The nature of the smectic A* phase of **5a**, **5b**, and **7a** was confirmed by X-ray diffraction. X-ray diffraction patterns typical for smectic phases were recorded (Figures 9, 11, and 13). In the small-angle region, several sharp reflections in the reciprocal spacing ratio 1:2:3 . . . were observed, corresponding to the lamellar periodicity (layer thickness) $L = 62$, 41, and 57 Å for **5a**, **5b**, and **7a**, respectively. The relative intensities of these reflections depend on the internal (electron density) structure of the stacked layers, of which the

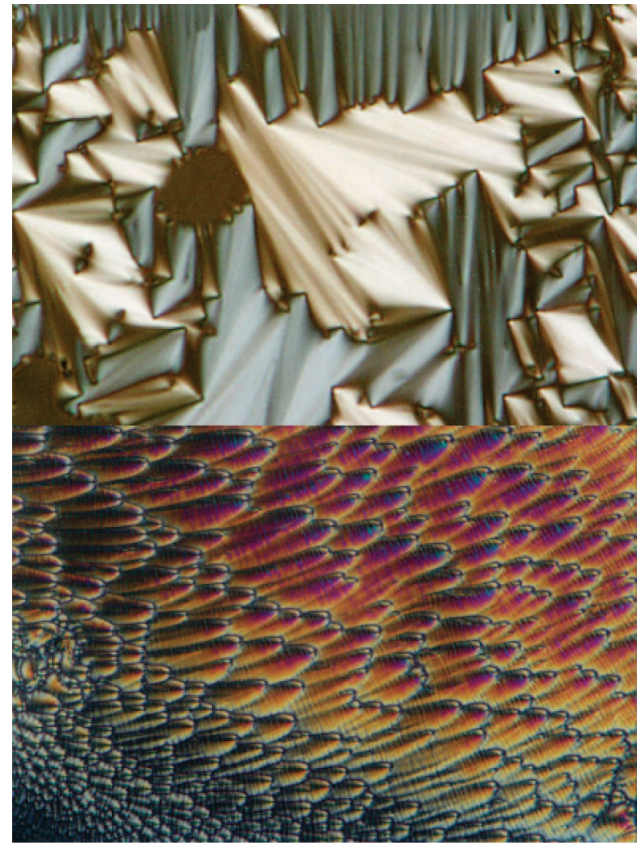

Figure 5. Top: fan texture of the SmA* phase of **5b** at 160 °C (500× magnification). Bottom: polygonal texture of the SmA phase of **6b** at 30 °C (500× magnification).

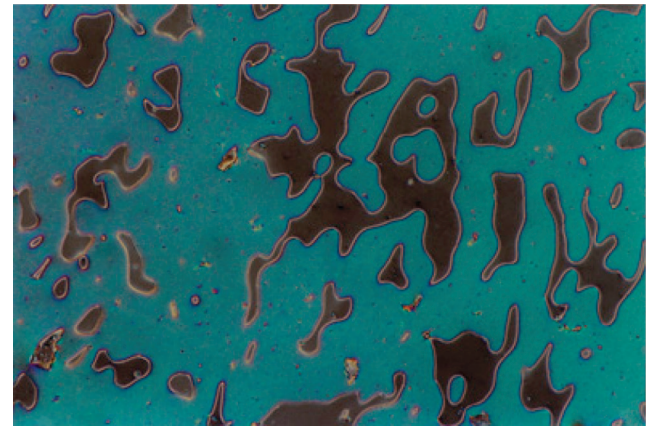

Figure 6. Threadlike texture of the nematic phase of **6b** at 44 °C (200× magnification).

modeling is introduced below. In addition, a diffuse signal was observed in the wide-angle region, centered at 4.5, 5.2, and 5.7 Å for **5a**, **5b**, and **7a**, respectively.

To give more information about the molecular organization within the smectic A* layers, the scattering patterns and the corresponding structures were modeled. The underlying theoretical and mathematical concepts are considered next.

The intensity for a single, isolated 1D lattice, $I_1(q)$, equals the product of the one-dimensional lattice interference function, $S(q)$, with the so-called *form factor*, $F(q)\,F^*(q)$.[74]

(74) *X-ray Diffraction by Disordered and Ordered Systems*; Hukins, D. W. L., Ed.; Pergamon Press: Oxford, United Kingdom, 1981.

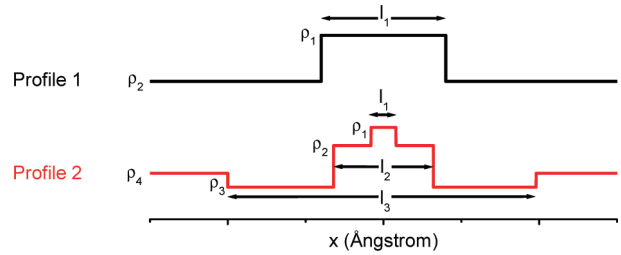

Figure 7. Electron density profiles of motifs with 2 (profile 1) and 4 (profile 2) electron density levels.

$$I_1(q) = S(q)\, F(q)\, F^*(q) \tag{1}$$

Here, q is the modulus of the scattering vector and is related to the scattering angle, 2θ, and the X-ray wavelength, λ, via

$$q = \frac{4\pi}{\lambda} \sin(\theta) \tag{2}$$

For a paracrystalline lattice, the function $S(q)$ can be written as[75]

$$S(q) = \frac{1 - \exp(-g^2q^2L^2)}{1 + \exp(-g^2q^2L^2) - 2\exp(-0.5g^2q^2L^2)\cos(qL)} \tag{3}$$

where the lattice repeat distance varies according to a Gaussian distribution around an average value L and with a width given by the parameter $g = \sigma_L/L$. σ_L is the standard deviation of the Gaussian distribution.

$F(q)$ is the scattering amplitude of the one-dimensional electron density profile, $\rho(x)$, that represents the repeated motif. $F(q)$ in the case of a symmetric blocklike motif (Figure 7, profile 1) with a length l_1 and an electron density ρ_1 inside and ρ_2 outside the motif reads

$$F(q) = \frac{2(\rho_2 - \rho_1)}{q} \sin\left(\frac{ql_1}{2}\right) \tag{4}$$

Since $F(q)$ in this case is a real function, it equals its complex conjugate, $F^*(q)$, and hence $F(q)\, F^*(q) = F(q)^2$. Equation 4 can be extended to motifs with n electron density levels according to

$$F(q) = \sum_{i=1}^{n-1} \frac{2(\rho_{i+1} - \rho_i)}{q} \sin\left(\frac{ql_i}{2}\right) \tag{5}$$

All distances l_i are defined symmetrically around the center of the structure, and the most central feature is l_1. The constraint holds that $l_i < l_{i+1}$. Profile 2 in Figure 8 illustrates the distances and densities associated with an arbitrary four-level electron density profile.

Additionally, the interfaces between the electron density levels can be made smoother by introducing transition layers with a thickness 3σ, as illustrated in Figure 8.

As a result, eq 5 modifies into[76]

$$F(q) = \sum_{i=1}^{n-1} \frac{2(\rho_{i+1} - \rho_i)}{q} \sin\left(\frac{ql_i}{2}\right) \exp(-0.5\sigma_i^2q^2) \tag{6}$$

Finally, the model needs to account for a (constant) background, B, and for the fact that the scattering patterns

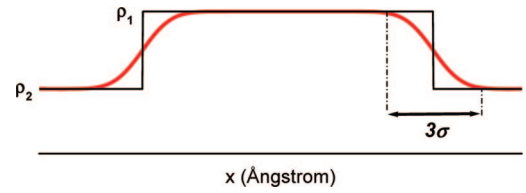

Figure 8. Two-level electron density profile without (black) and with (red) a transition zone of thickness 3σ.

are due to powders rather than isolated lattices (correction by multiplying with $1/(4\pi q^2)$) and that the intensities are not on an absolute scale (introduction of the scaling constant C):

$$I(q) = \frac{C}{4\pi q^2} S(q)\, F(q)^2 + B \tag{7}$$

Equation 7 was used in this work to fit the experimental scattering patterns. For $F(q)$, eq 6 was used. Fitting was done by minimizing the sum of squared differences between the experimental and theoretical (model) curves on a logarithmic scale (to enlarge the weight of small but important features in the scattering patterns). Rather than constructing electron density profiles from the resulting model parameters, it was decided to compute electron density profiles via a numerical Fourier cosine transformation of the obtained model $F(q)$ function:

$$\rho(x) = 2\int_0^\infty F(q) \exp(-0.5q^2) \cos(qx)\, dq \tag{8}$$

Integration was conducted over the range $0 \le q \le 4.2$ Å^{-1}. The exponential factor in the kernel of the integral reduces truncation errors. As a side effect, the interfaces in the electron density profiles received a small extra transition zone of 3 Å ($3\sigma = 3$ Å). This profile was then copied at integer multiples of L for visualization. Note that paracrystalline distortions are not considered in this representation mode. All mathematical handling was done in Microsoft Excel, and for fitting the built-in solver was used. At first, only the data below $2\theta = 10°$ were considered (the small-angle X-ray scattering or SAXS part), and all σ_i values were kept at zero. Variation of the σ_i values was only allowed in a last minimization cycle for fine-tuning but in most cases returned zero values. After all the smallest features that can be resolved in this SAXS region are about 8 Å. Electron density levels were introduced as long as this improved the fit and as as long as during the fitting procedure there was no spontaneous reduction to a lower number of electron density levels. The constraints $\rho_n = 0$ and $\rho_1 = 1$ were used (or vice versa: $\rho_n = 1$ and $\rho_1 = 0$). Occasionally, the data up to $2\theta = 30°$ were also fitted, resulting in an increased resolution up to 3 Å.

In Figure 9, the fitting results on the scattering pattern of **5a** (at 50 °C) are depicted. Figure 10 displays the corresponding electron density profiles together with a probable underlying molecular arrangement. The small-angle X-ray scattering (SAXS) part can be fitted satisfactorily by using four electron density levels (red curve in Figure 10). The central high electron density level is assigned to the bromide-containing ionic units. The low-density levels on both sides of the central layer are due to the aliphatic spacers and to

(75) Vignaud, R.; Schultz, J. M. *Polymer* **1986**, *27*, 651–658.
(76) Ruland, W. *J. Appl. Crystallogr.* **1971**, *4*, 70–73.

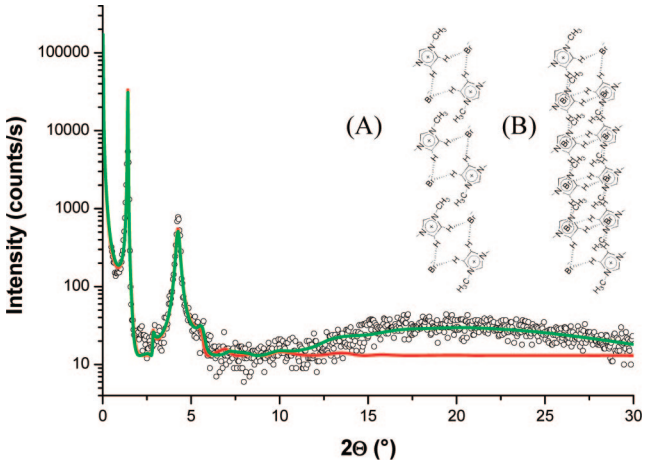

Figure 9. Results of fitting the scattering data (open circles; recorded at 50 °C) over the limited (red curve) and complete (green curve) angular range. Note that the function obtained by fitting over the SAXS range is extrapolated over the entire angular range (red curve). The insets illustrate a single layer of tilted, "stacking-compatible" imidazolium moieties of **5a** in (A) and two layers with facing opposite charges in (B).

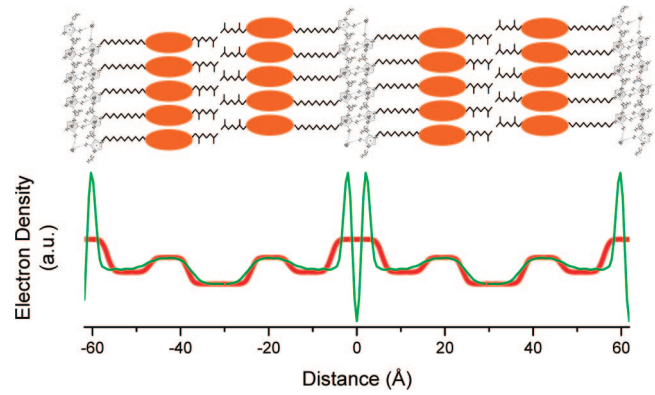

Figure 10. Electron density profiles for **5a** based on the fitting procedures over the limited (red curve: four electron density levels) and complete (green curve: five electron density levels with smooth transition zones) angular range. The profiles cover twice the layer thickness, *L*, i.e., twice 62 Å. The zero coordinate occurs in the center of the feature with the highest electron density in the red curve of which the molecular arrangement is explained in Figure 8. The cyclic parts of the cholesterol units are represented by orange ellipsoids of revolution. The aliphatic cholesterol tails and the aliphatic spacers with the ionic units are represented by simple sticks.

the high-density cyclic parts of the cholesterol units. Finally, the lowest density layers are due to the aliphatic cholesterol tails.

The dimensions of the different moieties in Figure 10 are fairly realistic. The end-to-end distances of the cyclic part of the cholesterol units along its longest and shortest axes are 10 and 5 Å, respectively. Upon rotation around its longest axis, ellipsoids of revolution are obtained with cross sections as illustrated by the orange features in Figure 10. For a proper lengthwise stacking of such ellipsoids, the imidazolium units need to be separated by a comparable 5 Å. In the insets to Figure 9 it is suggested that such a three-dimensional arrangement can be obtained by layers that stack on top of each other so that positive (imidazolium cation) and negative (bromide anion) charges are facing each other. Such a stacking of layers results in two bromide-rich planes in the central high-density layer of the one-dimensional lattice, separated by ~4.5 Å. Given the high bromide electron density, this molecular separation is expected to dominate the scattering pattern at higher angles. Following this line of thought, an extra electron density level was introduced, and the fitting range was extended to high angles. The result of the fit (green line in Figure 9) is satisfactory, and the envisaged molecular separation is reflected in the corresponding electron density profile (green line in Figure 10), indicating that indeed the mentioned bromide plane separation dominates the scattering pattern at higher angles. However, comparable inter-bromide distances can also be expected within the bromide planes, and also other interatomic interferences need to be accounted for in this part of the reciprocal space. Therefore, the good fit in terms of a strictly one-dimensional lattice at high angles is somehow artificial. On the other hand, it clearly demonstrates that interferences between heavy atoms dominate the scattering behavior at high angles. In fact, using Bragg's law, one can verify that a distance of 4.5 Å reflects at about 20° 2θ (in the case of Cu Kα radiation), which is at the maximum of the broad high-angle halo in Figure 9.

For a head-to-head arrangement of the molecules as proposed in Figure 10, the molecular area $A_M = 2V_M/L$ of an ionic cluster (consisting of two imidazolium cations and two bromide anions) can be deduced from the molecular volume ($V_M = 1187$ Å^3 at 50 °C, calculated using the relation $V_M = (M/0.6022)f$, where M is the molecular mass (g mol^{-1}) and f is a temperature correcting factor ($f = 0.9813 + 7.474.10^{-4}T$; T in °C))[77] and the layer thickness ($L = 62$ Å) and is found to be 38.3 Å^2. This value is close to that found for octylcholestane (37.7 Å^2 at 50 °C)[78] and supports the fact that the SmA* layers of **5a** are not interdigitated and that the cholesterol groups are not tilted, which is in complete agreement with the proposed model in Figure 10. The molecular organization of one layer is thus characterized by three sublayers of different chemical nature: a cholesteric sublayer, an ionic sublayer, and the layer consisting of the aliphatic continuum stemmed by the spacer. Microsegregation of compatible parts of the molecules and favorable interactions between these parts lead to the formation of smectic layers.

A similar arrangement with facing opposite charges was constructed for **5b**, as illustrated in the insets to Figure 11. Fitting of the SAXS range (at 100 °C) required only three electron density levels as illustrated in Figure 12. The lateral separation between the aliphatic spacers is increased as compared to **5a** (Figure 10) and is sufficiently wide to allow for an interdigitated cholesterol packing (Figure 12).

In contrast to the structure of **5a**, the central region of **5b** does not have the highest electron density. Therefore and because of the appropriate dimension, it was assigned to the interdigitated cholesterol units. The imidazolium containing layers need to have the highest electron density due to the presence of heavy sulfur atoms of the bis(trifluoromethylsulfonyl)imide anions. The fact that these layers are not in

(77) Felder-Flesch, D.; Rupnicki, L.; Bourgogne, C.; Donnio, B.; Guillon, D. *J. Mater. Chem.* **2006**, *16*, 304–309.
(78) Seurin, P.; Guillon, D.; Skoulios, A. *Mol. Cryst. Liq. Cryst.* **1980**, *61*, 185–189.

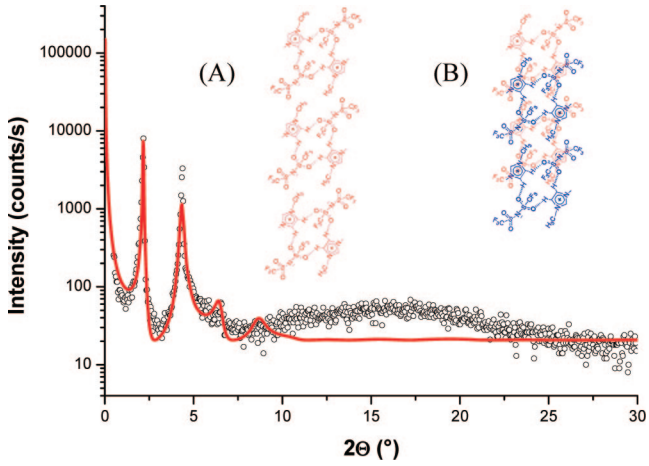

Figure 11. Result of fitting the scattering data (open circles; recorded at 100 °C) in the SAXS region and extrapolation of the result over the entire angular range (red curve). The insets illustrate a single layer of tilted, "stacking-compatible" imidazolium moieties of **5b** in (A) and two layers with facing opposite charges in (B).

the center implies that the paracrystalline disorder in the stacking of **5b** is mainly due to disorder in the imidazolium layers. The stacking disorder in **5a** originates from disorder in the cholesterol tails. This makes sense, as the interaction between these tails in the stack direction is very poor. The maximum of the broad high-angle halo in Figure 11, which must be due to a dominant inter-sulfur-atom distance, occurs at about $2\theta = 17°$ and corresponds to a distance of 5.2 Å.

As for **5a**, the molecular area $A_M = 2V_M/L$ of an ionic cluster can be deduced from the molecular volume (V_M = 1582 Å^3 at 100 °C) and the layer thickness (L = 41 Å) and is found to be 77.2 Å^2 in the case of **5b**. The molecular area is close to twice the transverse cross section of one cholesterol group. This supports the proposed model, for which the packing of the cholesterol moieties within the sublayers is described as a nontilted monolayer with strong interdigitation of the cholesterol groups from the molecules of adjacent layers (Figure 12). A cross-sectional area of 38.6 Å^2 per cholesterol group is deduced, which is consistent with the value found for octylcholestane. Thus, because of the large bis(trifluoromethylsulfonyl)imide anion, the molecular area of the ionic cluster is much larger than in the case of the corresponding bromide salt **5a**. This causes an interdigitation of the cholesterol groups.

Finally for **7a**, the high-angle halo (at 170 °C) is relatively intense and narrow with a maximum at $2\theta = 15.5°$, as can be seen in Figure 13. This reflects a well-ordered (long-range) bromide atom arrangement at a preferred distance of 5.7 Å. The ionic units of **7a** carry four aliphatic spacers to as many cholesterol units. In the insets to Figure 13 this is illustrated, and it is furthermore shown that for a positive–negative charge coupling, a simple two-layer construction is no longer sufficient. In contrast to **5a** and **5b**, the positions of the following two layers need to be arranged in such a way that they compensate the remaining charges. This results in a long-range ordered stairwise stacking of ionic units (and likely the observed maximum at $2\theta = 15.5°$). Obviously, because of the lower amount of ionic units in the associated layers, there is some space left to accommodate the linking alkyl chains, resulting in a smaller overall layer thickness,

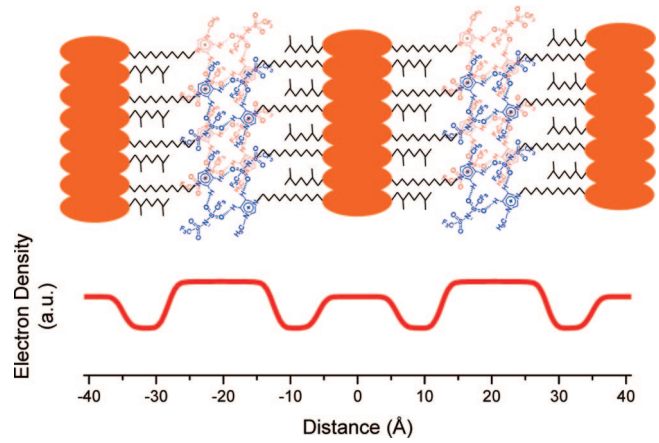

Figure 12. Electron density profile for **5b** based on a fitting of the SAXS data range (three electron density levels). The profile covers twice the layer thickness, L, i.e., twice 41 Å. Similar representation modes are used as in Figure 10 for the molecular model.

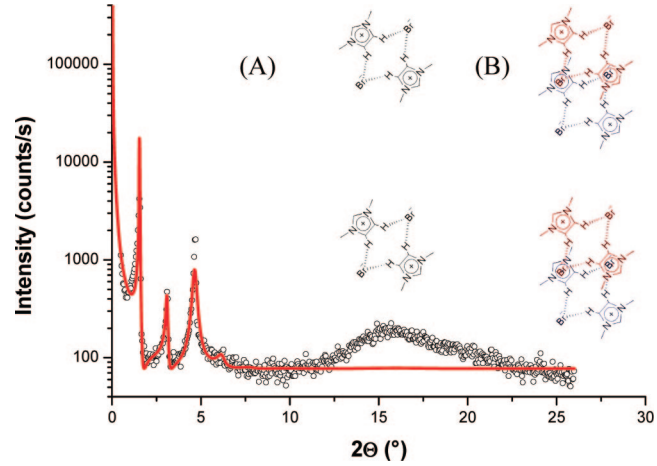

Figure 13. Result of fitting the scattering data (open circles; recorded at 170 °C) in the SAXS region and extrapolation of the result over the entire angular range (red curve). The insets illustrate a single layer of tilted, "stacking-compatible" imidazolium moieties of **7a** in (A) and two layers with facing opposite charges in (B).

L, compared to **5a**. Indeed, L reduces from 62 Å for compound **5a** to 57 Å for compound **7a**, as can be deduced from the scattering pattern and the corresponding electron density profile in Figures 13 and 14. Figure 14 also displays a possible molecular arrangement for compound **7a**. Note that the electron densities of the ionic layers for **7a** are rather low compared to those for **5a** in Figure 10. This is due to the reduced bromide content in the case of **7a**.

Again, by using the molecular volume (V_M = 2258 Å^3 at 170 °C) and the layer thickness (L = 57 Å), the molecular area of an ionic cluster was calculated as $A_M = 2V_M/L$ = 79.2 Å^2. As there are now two cholesterol groups per molecule, this gives a cross-sectional area per cholesterol group of 39.6 Å^2, supporting the model as proposed in Figure 14, for which the cholesterol groups of adjacent layers are not interdigitated. The molecular organization of **7a** is thus very similar to that of **5a**.

Finally, it is of interest to shortly discuss the stacking (dis)order via the parameter σ_L for the different compounds. (The other model parameters can be judged directly from the electron density profiles.) The σ_L values for **5a**, **5b**, and

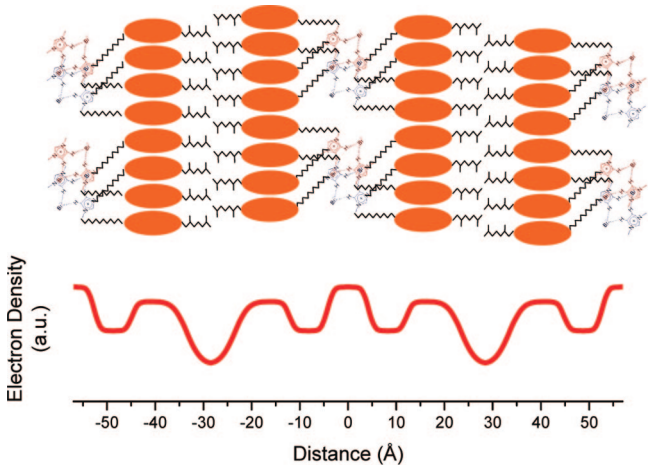

Figure 14. Electron density profile for **7a** based on a fitting of the SAXS data range (four electron density levels). The profile covers twice the layer thickness, *L*, i.e., twice 57 Å. Similar representation modes are used as in Figure 10 for the molecular model.

7a are 3.5, 2.6, and 3.2 Å, respectively. Clearly, the disorder in **5a** and **7a** is the largest because of the weak interactions between the cholesterol tails.

The concept of coupling mesogenic groups to various fragments via a long flexible spacer has been successful to produce liquid-crystalline C_{60} fullerenes,[79,80] octasilsesquioxanes,[81,82] high coordination number metal complexes of 1,10-phenanthrolines,[83] and lanthanide complexes of 2,6-bis(benzimidazole)pyridine.[84] In this study, we have shown that such a method is also fruitful to produce ionic liquid crystals containing large ionic metal fragments such as tetrakis(2-thenoyltrifluoroacetonato)europate(III). Recently, Pal and Kumar reported ionic liquid-crystalline dimers based on the imidazolium cation.[34] It is striking that their calamitic–calamitic dimer, which contains two cyanobiphenyl groups, shows a SmC phase. On the contrary, our bromide salt **6a**, for which the aliphatic spacer contains two carbon atoms more, shows a nematic phase (unequivocally assigned by POM; see above). This difference in phase behavior has to be due to the difference in spacer length. (The dependence of the transition temperatures and phase behavior on the spacer length of liquid-crystalline dimers and oligomers has been nicely covered by Imrie and Luckhurst.[85]) The presence of a nematic phase is remarkable because this weakly ordered phase is not expected for ionic liquid crystals. Traditionally, lamellar phases are observed for ionic systems because the strong, isotropic electrostatic forces stabilize a lamellar arrangement (whereas weak anisotropic dispersion forces stabilize the nematic phase).[24] The only other examples of (nonchiral) nematic ionic liquid crystals are the quaternary ammonium halide salts based on trioctadecylamine reported by Weiss and co-workers[86] and the silver(I) stilbazole complexes with short alkoxy chains reported by Bruce and co-workers.[87] However, the latter silver(I) complexes are only formally ionic because the compounds form tightly bound ion pairs.

Conclusions

Ionic liquid crystals were obtained by coupling mesogenic groups to a cationic imidazolium core. The thermal behavior of these mesogens depends on the number of mesogenic units attached to the imidazolium cation, the type of mesogenic promoter, and the type of counterion. In general, the most stable mesophases were observed for the bis(trifluoromethylsulfonyl)imide salts, and it turned out that the cholesterol group is a stronger mesogenic promoter than the cyanobiphenyl group for this system. Enantiotropic SmA* phases were observed for almost all cholesterol-containing compounds, some of them being liquid crystalline even at room temperature. However, by coupling two cyanobiphenyl groups to the imidazolium unit, nematic phases were observed. This approach to nematogenic ionic liquid crystals will be extended to other mesogenic groups, other heterocyclic cores, and other anions. Luminescent ionic liquid crystals could be obtained using tetrakis(2-thenoyltrifluoroacetonato)europate(III) as anion and by attaching two cholesterol groups to counterbalance the bulky ionic metal fragment.

Acknowledgment. T.C., K.D., and B.G. thank the FWO-Flanders for a postdoctoral fellowship. K.G. is research assistant of the FWO-Flanders. K.B. thanks the FWO-Flanders (project G.0508.07) and the K.U.Leuven (projects GOA 03/03 and IDO/05/005). The authors thank Dr. Bertrand Donnio and Dr. Daniel Guillon (IPCMS, Strasbourg, France) for useful discussions. ^{13}C NMR spectra were recorded by Karel Duerinckx. CHN analyses were performed by Dirk Henot. Mass spectra were measured by Bert Demarsin.

Supporting Information Available: Synthesis and characterization of the precursors **1–3**, europium(III) triflate, and compound **8**; packing of **4a** and **8** in the crystal structure and CIF files of the crystal structures; polarizing optical microscopy textures. This material is available free of charge via the Internet at http://pubs.acs.org.

CM702321C

(79) Dardel, B.; Deschenaux, R.; Even, M.; Serrano, E. *Macromolecules* **1999**, *32*, 5193–5198.
(80) Even, M.; Heinrich, B.; Guillon, D.; Guldi, D. M.; Prato, M.; Deschenaux, R. *Chem.—Eur. J.* **2001**, *7*, 2595–2604.
(81) Saez, I. M.; Goodby, J. W.; Richardson, R. M. *Chem.—Eur. J.* **2001**, *7*, 2758–2764.
(82) Saez, I. M.; Goodby, J. W. *J. Mater. Chem.* **2005**, *15*, 26–40.
(83) Cardinaels, T.; Driesen, K.; Parac-Vogt, T. N.; Heinrich, B.; Bourgogne, C.; Guillon, D.; Donnio, B.; Binnemans, K. *Chem. Mater.* **2005**, *17*, 6589–6598.
(84) Terazzi, E.; Bocquet, B.; Campidelli, S.; Donnio, B.; Guillon, D.; Deschenaux, R.; Piguet, C. *Chem. Commun.* **2006**, 2922–2924.
(85) Imrie, C. T.; Luckhurst, G. R. Liquid Crystal Dimers and Oligomers. In *Handbook of Liquid Crystals*; Demus, D., Goodby, J. W., Gray, G. W., Spiess, H.-W., Vill, V., Eds.; Wiley-VCH: Weinheim, Germany, 1998; pp 801–802.
(86) Lu, L.; Sharma, N.; Gowda, G. A. N.; Khetrapal, C. L.; Weiss, R. G. *Liq. Cryst.* **1997**, *22*, 23–28.
(87) Bruce, D. W. *Acc. Chem. Res.* **2000**, *33*, 831–840.